Petroleum Science 23 (2026) 5174–5188

Contents lists available at ScienceDirect

Petroleum Science

journal homepage: www.keaipublishing.com/en/journals/petroleum-science

Original Paper

Investigation of hydrocyclone coupled with particles for enhancing oil–water separation

Shuang Zhang [a,b], Li-Xin Zhao [a,b,c,*], Xing-Yue Chen [a,b], Lin Liu [a,b], Ming-Hu Jiang [a,b]

[a] School of Mechanical Science and Engineering, Northeast Petroleum University, Daqing, 163318, Heilongjiang, China
[b] Heilongjiang Key Laboratory of Petroleum and Petrochemical Multiphase Treatment and Pollution Prevention, Daqing, 163318, Heilongjiang, China
[c] State Key Laboratory of Continental Shale Oil, Daqing, 163318, Heilongjiang, China

ARTICLE INFO

Article history:
Received 19 August 2025
Received in revised form
1 November 2025
Accepted 23 March 2026
Available online 26 March 2026

Edited by Min Li

Keywords:
Multiphase coupling
Hydrocyclone
Adhesion
Fine oil droplets
Enhanced separation

ABSTRACT

Efficient oil-water separation is essential for treating produced fluids in petroleum engineering. This study investigates performance enhancement in hydrocyclones coupled with particles through theoretical analysis, visualization experiments, and numerical simulations. A critical model for oil droplet-particle collisions was established, revealing that smaller particle diameter, larger rotational radius, and smaller contact angle favor stable adsorption. Visualization experiments confirmed that particles promote droplet migration toward the hydrocyclone center, forming stable droplet-particle complexes at low rotational speeds while rebound dominates at higher speeds. A discrete element model based on the Johnson-Kendall-Roberts (JKR) adhesion theory was developed and validated, achieving a repose angle error of only 0.24%. Numerical results demonstrate that oleophilic particles significantly enhance droplet adhesion and improve overall separation efficiency by 8.19 percentage points, achieving 79.23% efficiency for 67 μm droplets (29.68 points higher than conventional hydrocyclones). These findings offer theoretical and practical support for optimizing and applying hydrocyclones coupled with particles in oilfield fluid treatment.

1. Introduction

In recent years, most oilfields around the world have entered the high-water-cut stage, characterized by a sharp increase in the water content of produced fluids. With the continuous growth of oil and gas extraction activities, the global volume of oilfield produced water has risen significantly, making the treatment of oily wastewater a pressing environmental concern (Amakiri et al., 2022; Chen et al., 2020; Patel et al., 2020). Among various multiphase separation methods, physical separation technologies are often preferred due to their operational simplicity, environmental friendliness, and low cost. Common physical treatment methods include gravity settling, filtration, and hydrocyclone separation (César et al., 2025; Fu et al., 2020; Xu et al., 2021). In particular, hydrocyclone separation has gained broad attention in the field of produced fluid pre-treatment due to its simple structure, fast separation, small volume and low operational and maintenance costs (Liu et al., 2018; Kharoua et al., 2010; Gao et al., 2022).

A hydrocyclone utilizes the high-speed swirling flow to generate a strong centrifugal field, enabling spatial separation of immiscible phases with density differences (Yang et al., 2023; E et al., 2025; Pukkella et al., 2025). Oil droplets with lighter density typically migrate toward the central axis and are discharged through the overflow outlet, while the water phase and denser contaminants are directed toward the wall and discharged through the underflow outlet. However, with increasingly stringent environmental regulations and the advancement of some oilfield development into the mid-to-late production stage, new technical challenges have emerged. In some mature oilfields, the density difference between oil and water is typically small, especially in heavy oil production. For polymer-flooded systems, severe oil droplet emulsification further complicates separation. As a result, relying solely on centrifugal force often leads to incomplete separation, and the oil content in the underflow stream frequently fails to meet reinjection or other technological standards.

To improve the separation efficiency of fine dispersed phases, several enhanced hydrocyclone technologies have been proposed. Mini-hydrocyclones can effectively enhance the separation of fine

* Corresponding author.
E-mail address: Lxzhao@nepu.edu.cn (L.-X. Zhao).
Peer review under the responsibility of China University of Petroleum (Beijing).

https://doi.org/10.1016/j.petsci.2026.03.047
1995-8226/

particles and oil droplets; however, this improvement is often accompanied by a significant increase in energy consumption (Dai et al., 2025; Lu et al., 2024; Liu et al., 2022). Gas-assisted hydrocyclones have also been developed by integrating flotation and centrifugal separation techniques, which utilize bubbles to promote oil droplet attachment and migration. Nevertheless, challenges associated with bubble size instability and bubble disappearance during operation remain unresolved (Liu et al., 2024b). Furthermore, fiber-coupled hydrocyclones have recently shown promising results in improving fine droplet coalescence and separation efficiency (Zhang et al., 2025). Despite these advances, the effective removal of microfine oil droplets remains a key challenge that must be addressed for the broader application of hydrocyclone technology (Wang et al., 2024; Ekechukwu et al., 2024).

To address this challenge, researchers have proposed a hydrocyclone coupled with particles separation method (Liu et al., 2019). This approach enhances separation without introducing additional physical fields or chemical additives, but rather by injecting low-density particles with diameters larger than that of the oil droplets into the multiphase mixture. These particles migrate from the periphery toward the center and upwards from the bottom, forming a dynamic particle film within the hydrocyclone. This film can adsorb and carry fine oil droplets through reverse interception and co-migration, thereby significantly improving the separation efficiency. Previous studies have demonstrated the feasibility of this approach: Liu et al. successfully used magnetically responsive particles to drive oil droplets toward the central axis, enhancing oil-water separation (Liu et al., 2019), meanwhile, Zhang et al. analyzed particle-droplet interactions and confirmed the coupling advantages of this method (Zhang et al., 2023).

Despite the recent development of hydrocyclone separation coupled with particles, the underlying mechanisms of multiphase coupling remain insufficiently understood, especially under strongly turbulent conditions (Zhao et al., 2025). Analyzing the motion and interaction forces between particles and droplets in the flow field is essential to understanding the fundamental physics of this novel separation method. The collision between a droplet and a solid particle can be regarded as a free-surface flow of liquid on a solid substrate, which represents a typical unsteady flow problem (Fan et al., 2023). The free-surface flow behavior involves multiple physical aspects, and the outcome of droplet–particle collisions is influenced by several key parameters, including collision velocity and direction, fluid properties (density, viscosity, and surface tension), droplet and particle sizes, and solid surface characteristics (such as roughness and wettability) (Mitra et al., 2017; Malgarinos et al., 2016; Bordbar et al., 2018).

However, most existing studies on particle interactions have focused on two-particle systems under low Reynolds number conditions. In contrast, information on particle–droplet interactions under highly turbulent flow fields remains relatively limited, as the motion of both phases becomes more complex and is governed by a wider range of coupled factors. Overall, the interaction mechanisms between particles and droplets in highly turbulent flow environments are still not fully understood. A deeper investigation into the motion, collision behavior, and resulting effects of particles and droplets in such fields remains a critical challenge that needs to be addressed.

This study aims to investigate the collision and adsorption mechanisms between oil droplets and lipophilic particles within a hydrocyclone field, and to develop a discrete-phase simulation model capable of accurately capturing these interactions under highly turbulent conditions. In addition, the study aims to elucidate the coupling mechanism involved in particle-enhanced hydrocyclone separation and to demonstrate the effectiveness and application potential of hydrocyclone coupled with particles for oil-water separation, particularly in the removal of fine oil droplets.

2. Materials, methods, and hydrocyclone configuration

2.1. High-speed visualization experiment

To investigate the motion behavior of particles and oil droplets, as well as the collision and adsorption phenomena in the coupling field, a high-speed imaging-based visualization system was developed, as illustrated in Fig. 1(a). The system generates a swirling field driven by a magnetic stirrer and is equipped with a high-speed camera (Olympus I-speed-3-T2, up to 150,000 fps), a lighting system, and a light-shielding panel for capturing the dynamic interactions between oil droplets and particles, as shown in Fig. 1(b). The test materials used were 1.5 mm polypropylene particles and gear oil. The gear oil used in the visualization experiment had a density of 905 kg/m^3, a dynamic viscosity of 0.285 Pa·s, and an interfacial tension against water of 0.031 N/m at 25 °C.

During the experiment, a magnetic rotor and distilled water were placed in a beaker. After stabilizing the temperature and rotation speed of the stirrer (diameter = 70 mm), oil droplets and particles were sequentially introduced. The stirring speed was adjusted between 800 and 1200 r/min so that the Reynolds number of the swirling flow field was of the same order of magnitude as that inside a hydrocyclone, ensuring dynamic similarity between the two systems. The swirling flow field produced by the magnetic stirrer has been demonstrated in previous studies to effectively replicate the internal vortex structure and droplet migration behavior of hydrocyclones (Mahmud et al., 2009; Xing et al., 2023). By adjusting the lighting and camera parameters, the motion, collision, and coalescence/adsorption behavior of oil droplets and particles were recorded, as shown in Fig. 2. Image analysis focused on the observation region to track the motion characteristics of oil droplets, particles, gas nuclei, and the resulting particle-droplet aggregates, thereby providing experimental support for validating the theoretical model.

2.2. Numerical simulation

2.2.1. Geometric model and mesh generation

A double-cone hydrocyclone with a main diameter of $D_1 = 36$ mm was selected as the model for numerical analysis. The geometric configuration of the hydrocyclone is illustrated in Fig. 3, and its primary structural dimensions are listed in Table 1. The hydrocyclone consists of two tangential inlets, a cylindrical section, a large cone section, a small cone section, an overflow pipe, and an underflow pipe (Fatahian et al., 2021; Liu et al., 2024a).

To ensure the accuracy of the numerical simulations, a grid independence study was conducted using four different mesh densities: 373,946, 484,892, 647,630, and 750,372 cells. Grid details and grid quality check are shown in Fig. 4(a) and (b). The pressure drop (ΔP) at the overflow outlet were used as the evaluation criteria. As shown in Fig. 4(c), the pressure drop stabilizes when the mesh count reaches 484,892, indicating that further increasing the grid resolution has a negligible impact on simulation accuracy. Considering both accuracy and computational efficiency, a mesh with 647,630 cells was selected for subsequent simulations.

2.2.2. CFD-DEM coupling method

Due to the limitations of using a single simulation method, traditional CFD or DEM approaches are insufficient for

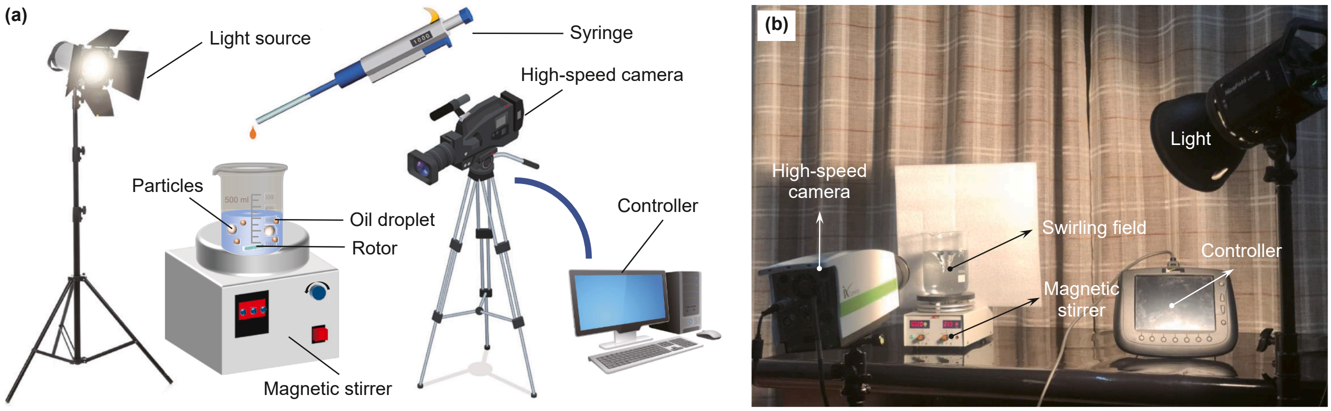

Fig. 1. Visualization experimental system.

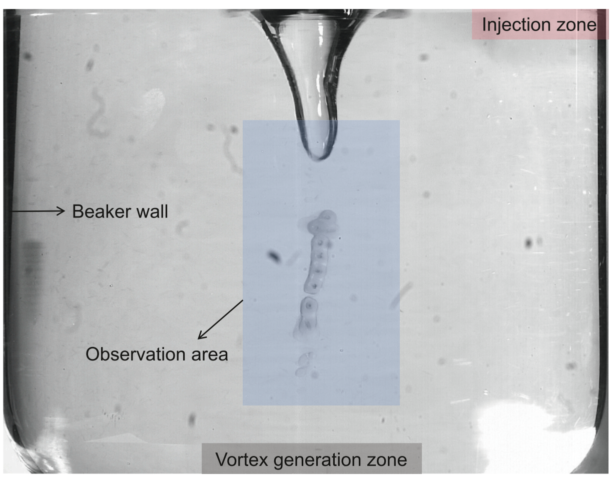

Fig. 2. Visualization experimental system.

independently and accurately modeling complex solid–liquid multiphase flows (Hou et al., 2022; Deng et al., 2013; Bhamjee et al., 2022; Zhou et al., 2019). In contrast, the coupled CFD-DEM method leverages the strengths of both techniques, enabling a more precise representation of discrete phase motion and its interaction with the continuous flow field.

In this study, EDEM was employed to simulate the motion of discrete-phase particles and oil droplets, while ANSYS Fluent was used to compute the continuous-phase water flow. The Eulerian-Lagrangian framework was adopted, where the continuous phase was governed by the Reynolds Stress Model (RSM) to capture the strong anisotropy and swirling characteristics of the internal flow field. The pressure-velocity coupling was handled using the SIMPLE algorithm, and the second-order upwind scheme was applied for discretizing the convective terms. The inlet boundary of the hydrocyclone was defined as a velocity inlet with a specified velocity of 10.42 m/s (Zhang et al., 2023), and the outlet boundary was set as a velocity outlet. The overflow split ratio, defined as the ratio of overflow discharge to total inlet flow rate (Xing et al., 2022; Tian et al., 2018), was set to 20%.

The oil droplets were modeled as spherical with a density (ρ_o) of 905 kg/m^3, and their diameters followed a normal distribution ranging from 50 to 300 μm, with a median size of 125 μm. The particle diameters were set to 355 μm. Oil droplets and solid particles were introduced into the hydrocyclone by mixing with the continuous water phase at 0 and 0.15 s, respectively. The oil droplets were injected near the inlet region at a mass flow rate of 0.00188 kg/s, while the solid particles were generated at a mass

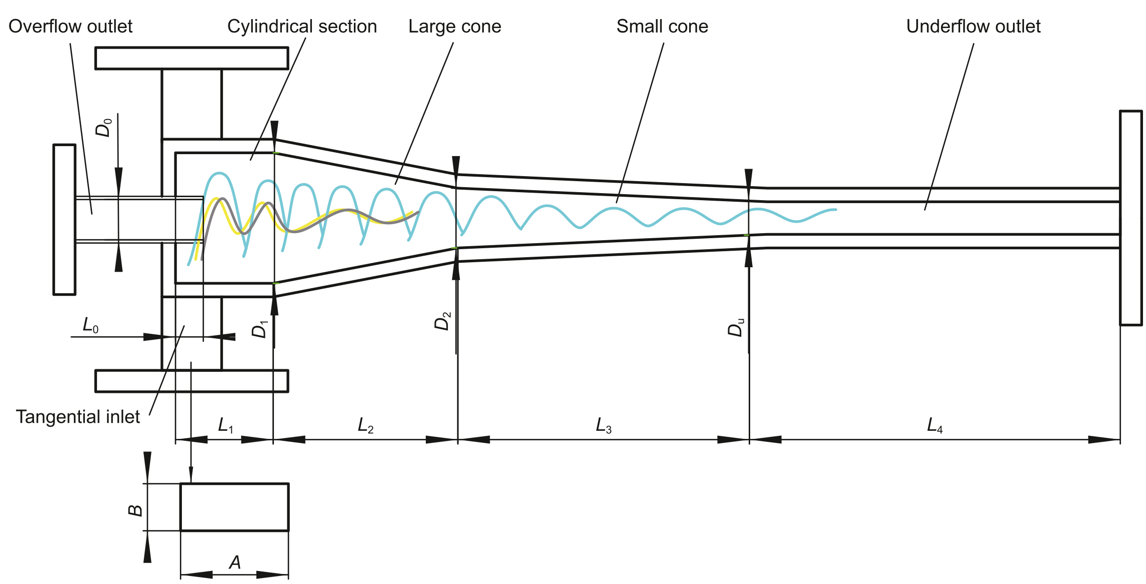

Fig. 3. Hydrocyclone geometric model.

Table 1
Main dimensions of hydrocyclone model.

D_o/D_1	D_2/D_1	D_u/D_1	A/D_1	B/D_1	L_1/D_1	L_o/D_1	L_2/D_1	L_3/D_1	L_4/D_1
0.125	0.23	0.13	0.28	0.11	0.75	0.45	1.42	2.375	2.70

flow rate of 0.00111 kg/s. A time step of 2×10^{-7} s was used in EDEM, accounting for about 25% of the Rayleigh critical time step. The Fluent time step was set to 1×10^{-6} s (5 times that of EDEM). A convergence criterion of 1×10^{-6} was applied to ensure computational accuracy.

2.3. Calibration of adhesion parameters

The Hertz-Mindlin with JKR (Johnson-Kendall-Roberts) model is an advanced particle contact mechanics model that combines the Hertz-Mindlin contact theory with the JKR adhesion theory (Li et al., 2022; Gao, 2018; Shahzad et al., 2018). It simultaneously accounts for normal forces, tangential forces, and the influence of surface energy (γ) on inter-particle adhesion, thereby enabling accurate characterization of the complex contact behavior between wet particles. As the JKR surface energy coefficient varies significantly with particle material and size, system-specific calibration is necessary. In this study, the surface energy coefficient of polypropylene (PP) particles was calibrated by combining stacking tests with numerical simulations to quantify their adhesive interactions with oil droplets.

2.3.1. JKR adhesive contact model

The JKR normal contact force depends on the overlap ζ and surface energy γ, as described by:

$$F_{\text{jkr}} = -4\sqrt{\pi\gamma E^* r^{3/2}} + \frac{4E^*}{3R^*}r^3 \quad (1)$$

$$\zeta = \frac{\alpha^2}{R^*} - \sqrt{\frac{4\pi\gamma\alpha}{E^*}} \quad (2)$$

where r is the contact radius, E^* is the equivalent Young's modulus, and R^* is the equivalent radius. The equivalent parameters are defined as:

$$\frac{1}{E^*} = \frac{\left(1-\nu_i^2\right)}{E_i} + \frac{\left(1-\nu_j^2\right)}{E_j} \quad (3)$$

$$\frac{1}{R^*} = \frac{1}{R_i} + \frac{1}{R_j} \quad (4)$$

where E_i, ν_i, R_i and E_j, ν_j, R_j denote the Young's modulus, Poisson's ratio, and radius of the two contacting particles i and j, respectively.

Even when the particles are not in physical contact, the Hertz-Mindlin with JKR model introduces cohesive forces between them. The maximum separation distance at which a non-zero adhesive force exists is given by:

$$\zeta_c = -\sqrt{\frac{4\pi\gamma r_c}{E^*}} + \frac{r_c^2}{R^*} \quad (5)$$

$$r_c = \left[\frac{9\pi\gamma R^{*2}}{2E^*}\left(\frac{3}{4} - \frac{1}{\sqrt{2}}\right)\right]^{\frac{1}{3}} \quad (6)$$

For $\zeta < \zeta_c$, the model returns zero force. When the separation between particles is smaller than $|\zeta_c|$ but they are not in direct contact, a maximum cohesive force—also known as the pull-off force—occurs. This represents the maximum tensile force required to separate two particles until no interaction remains, and it can be expressed as:

$$F_{\text{pull out}} = -\frac{3}{2}\pi\gamma R^* \quad (7)$$

Although originally developed for fine dry particles, the JKR model can also describe wet particle interactions. In this case, the separation force between two particles depends on the liquid surface tension γ_s and the contact angle α:

$$F'_{\text{pull out}} = 2\pi\gamma_s \cdot \cos\alpha\sqrt{R_i R_j} \quad (8)$$

By equating this force with the JKR pull-off force $F_{\text{pull out}}$, the surface energy γ in the JKR model can be estimated, enabling quantitative calibration of interparticle adhesion strength.

2.3.2. Angle of repose—physical measurement

The angle of repose refers to the slope formed when particles naturally accumulate and serves as a macroscopic parameter for characterizing particle flow behavior. It is commonly used as an indicator for calibrating particle-related parameters (Cunha et al., 2016; Zhou et al., 2022). The stacking test is a widely adopted method for measuring the angle of repose. In this study, polypropylene (PP) pellets were provided by Hengfa Plasticizing Co., located in Dongguan, China. PP particles with sizes ranging from 355 to 400 μm were selected using 50- and 45-mesh sieves for the stacking test. The test apparatus is shown in Fig. 5(a).

The specific procedure for the stacking test is as follows: during the measurement, the prepared oil-containing particles were slowly poured into the funnel and gently stirred with a glass rod to prevent clogging at the outlet. Once a sufficient quantity of particles had accumulated in the glass dish, the addition was stopped. When the height of the particle heap stabilized, a front-view image was captured using a camera. Image processing was then performed to calculate the angle of repose. The steps included grayscale conversion, binarization, noise reduction, edge detection, and linear fitting. The slope of the fitted line was used to calculate the tangent of the repose angle, as expressed in Eq. (9) (Han et al., 2023).

$$\beta = \frac{\arctan|k| \times 180^\circ}{\pi} \quad (9)$$

where, β represents the measured angle of repose, and k the slope of the fitted line.

Five independent stacking tests were conducted, and the average measured angle of repose was 52.50°.

2.3.3. Angle of repose—numerical simulation

Based on the physical properties of polypropylene (PP) particles and gear oil, as well as the discrete element simulation parameter settings for stainless steel materials reported in the literature (Han et al., 2023; Lupo et al., 2021), the simulation parameters used in this study are listed in Table 2. The virtual simulation of the angle of repose followed a procedure similar to that of the physical test. In the hopper, a dynamic virtual environment randomly generated particles and oil droplets. The oil-containing particles flowed out from the bottom of the hopper and gradually formed a pile, as shown in Fig. 5(b), thereby replicating the conditions of the stacking test. Once a distinct heap was formed, particle generation ceased. After all particles had stabilized, the angle of repose was measured. At this point, the particle pile exhibited a truncated cone shape.

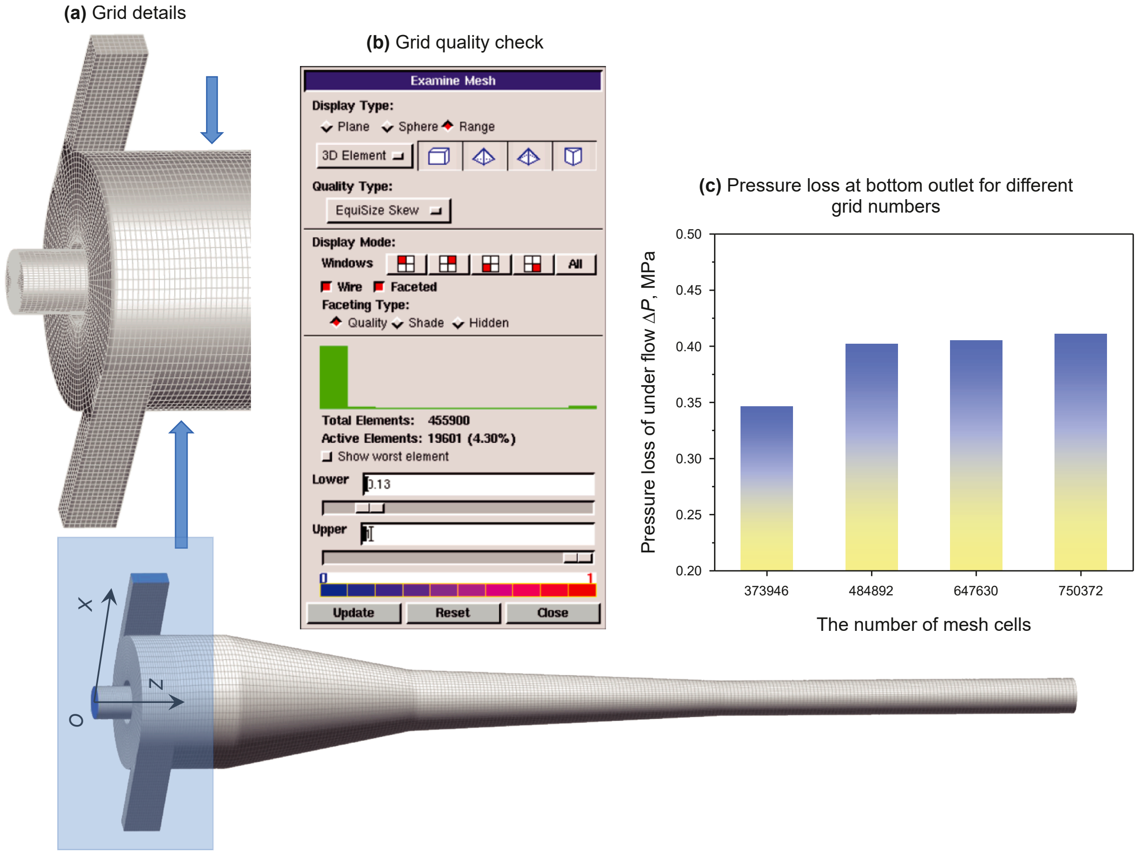

Fig. 4. Hydrocyclone grid division and independence verification.

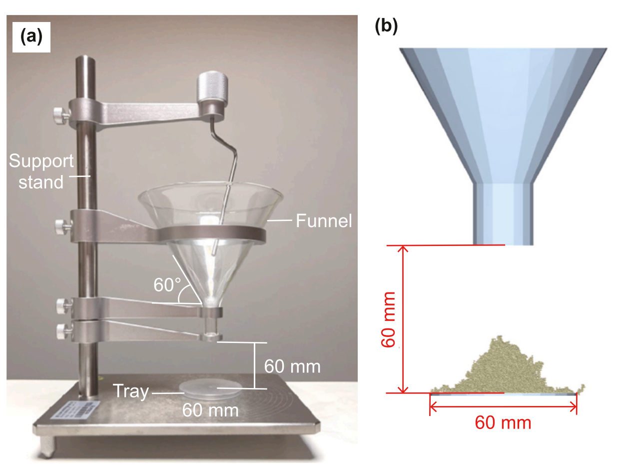

Fig. 5. Repose angle measurement setup. (**a**) Physical test; (**b**) simulation test.

2.3.4. Model validation

In this study, the JKR surface energy coefficients between oil-coated particles were determined through parameter calibration tests, which consisted of two stages. First, a steepest ascent experiment was conducted to explore the optimal ranges of JKR parameters: J_p (between PP particles), J_{op} (between particles and oil droplets), and J_o (between oil droplets). Based on preliminary simulation trials, their respective ranges were set to 0.05–0.3 J/m^2, 5–7.5 J/m^2, and 6–8.5 J/m^2. The specific experimental design and results are shown in Table 3. Simulation results indicated that the parameter combination ($J_p = 0.25$, $J_{op} = 7$, $J_o = 8$) yielded the smallest relative error (2.95%) between the simulated and experimental angle of repose. This combination was therefore selected as the center point for the subsequent Box-Behnken design (BBD). The design matrix and the corresponding results for each run are presented in Table 4. A second-order regression model was then established to correlate the JKR parameters with the angle of repose. The model demonstrated strong goodness of fit, with an R^2

Table 2
Parameters required in DEM simulation.

Parameter	Value	Parameter	Value
Particle density, kg/m^3	890	Particle–particle restitution coefficient	0.15
Oil droplet density, kg/m^3	905	Particle–particle static friction coefficient	0.20
Particle Poisson's ratio	0.25	Particle–particle rolling friction coefficient	0.50
Particle shear modulus, Pa	2.7×10^7	Particle–stainless steel restitution coefficient	0.20
Stainless steel density, kg/m^3	7800	Particle–stainless steel static friction coefficient	0.50
Stainless steel Poisson's ratio	0.30	Particle–stainless steel rolling friction coefficient	0.80
Stainless steel shear modulus, Pa	7.0×10^{10}		

Table 3
Design and simulation results of the steepest ascent test.

	Factor			Angle of repose, °	Relative error, %
	J_p, J/m^2	J_{op}, J/m^2	J_o, J/m^2		
1	0.1	5.5	6.5	32.44	38.21
2	0.15	6	7	40.01	23.79
3	0.2	6.5	7.5	47.37	9.77
4	0.25	7	8	54.05	2.95
5	0.3	7.5	8.5	59.12	12.61

Table 4
BBD experimental design and result statistics.

	J_p, J/m^2	J_{op}, J/m^2	J_o, J/m^2	Angle of repose, °	Relative error, %
1	−1	−1	0	49.17	5.7
2	0	1	1	57.66	10.59
3	1	0	−1	50.73	2.70
4	−1	0	−1	48.76	6.44
5	1	0	1	54.76	5.03
6	1	−1	0	49.82	4.46
7	0	0	0	54.05	3.66
8	0	1	−1	51.35	1.5
9	−1	0	1	53.80	3.18
10	0	0	0	54.05	3.66
11	0	−1	1	52.08	0.74
12	0	−1	−1	50.44	3.26
13	1	1	0	55.08	5.64
14	−1	1	0	52.56	0.8
15	0	0	0	54.05	3.66

of 0.9923 and a p-value < 0.0001, indicating a statistically significant result.

Using Design Expert software for optimization, the optimal JKR parameter set was determined to be $J_p = 0.272$, $J_{op} = 6.74$, and $J_o = 7.75$. The simulation conducted with this optimized parameter set produced an angle of repose with only a 0.24% error compared to the experimental value, as shown in Fig. 6. These results confirm that the JKR model can effectively describe the adhesive interactions between particles and oil droplets, and is suitable for simulating multiphase coupling behaviors in hydrocyclone systems coupled with particles for enhanced oil-water separation.

3. Results and discussion

3.1. Theoretical analysis

In the hydrocyclone field, the interfacial stability of oil droplets adhering to particle surfaces is influenced by multiple critical factors, including collision velocity and direction, fluid properties (e.g., density, viscosity, and surface tension), solid surface characteristics (e.g., roughness and wettability), and the sizes of both oil droplets and particles. Under different collision conditions, dynamic behaviors such as spreading, deformation, rebound, or adhesion may occur, directly determining the outcomes of droplet–particle interactions (Dalgamoni and Yong, 2021).

Before contact occurs, as shown in Fig. 7(a), both particles and oil droplets in the hydrocyclone field are subjected to multiple forces. In the radial direction, these include the centrifugal force (F_C), pressure gradient force (F_P), Stokes drag (F_S) from the continuous water phase, and the Magnus force (F_M) generated by droplet rotation. In the axial direction, the oil droplet is mainly influenced by its own gravity (F_g), buoyant force (F_b), and axial drag force (F_s). These forces collectively determine the trajectories and collision probabilities of oil droplets and particles within the hydrocyclone.

At the moment of contact, the droplet's kinetic energy becomes dominant, and inertial force governs the impact dynamics. The interplay between kinetic and surface energies determines whether the droplet stably spreads (adheres) or rebounds from the particle surface. Neglecting friction between the droplet and the particle, the energy relationship during the initial collision and at the maximum spreading state can be described by the conservation of energy (Fan et al., 2023):

$$E_s + E_k + E_p = E_{ow} + E_{op} + E_{pp} + E_{vd} \tag{10}$$

where, E_s, E_k and E_p represent the initial surface energy, kinetic energy, and potential energy of the oil droplet, respectively; E_{ow} is the oil-water interfacial energy, E_{op} is the oil-particle interfacial energy, E_{pp} is the potential energy at maximum spreading, and E_{vd} is the viscous dissipation energy.

The initial surface energy E_s, kinetic energy E_k, and potential energy E_p can be expressed as follows:

$$E_s = \pi x_o^2 \sigma_{ow} \tag{11}$$

$$E_k = \frac{1}{2} m_o v^2 = \frac{\pi}{12}\rho_l v^2 x_o^3 = \frac{\pi}{12} We \cdot \sigma_{ow} D_o^2 \tag{12}$$

$$E_p = m_o g \left(x_p + \frac{1}{2} x_o \right) \tag{13}$$

where σ_{ow} represents the interfacial tension between the oil droplet and the surrounding liquid; x_o is the oil droplet diameter; and x_p denotes the particle diameter.

At the maximum spreading state of the oil droplet, the interfacial energy of the liquid–liquid interface E_{ow} can be expressed as:

$$E_{ow} = A_{ow}\sigma_{ow} = 2\pi \times R(R-H) \times \sigma_{ow} = 2\pi\sigma_{ow} R(R-H) \tag{14}$$

where A_{ow} is the contact area between the oil droplet and the liquid, R denotes the radius of curvature of the spherical cap formed by the droplet after spreading, and $R = x_p/2 + h$.

It is assumed that the liquid–liquid interfacial area of the oil film is equal to the outer surface area of a particle with radius R and

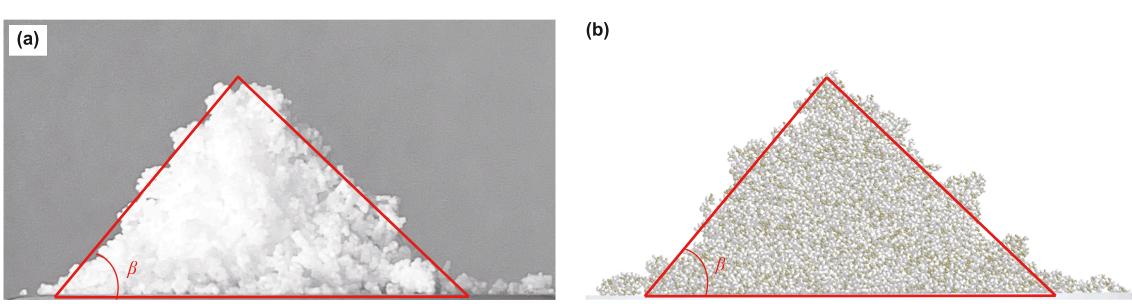

Fig. 6. Comparison of simulation and physical tests. (**a**) Physical test; (**b**) simulation test.

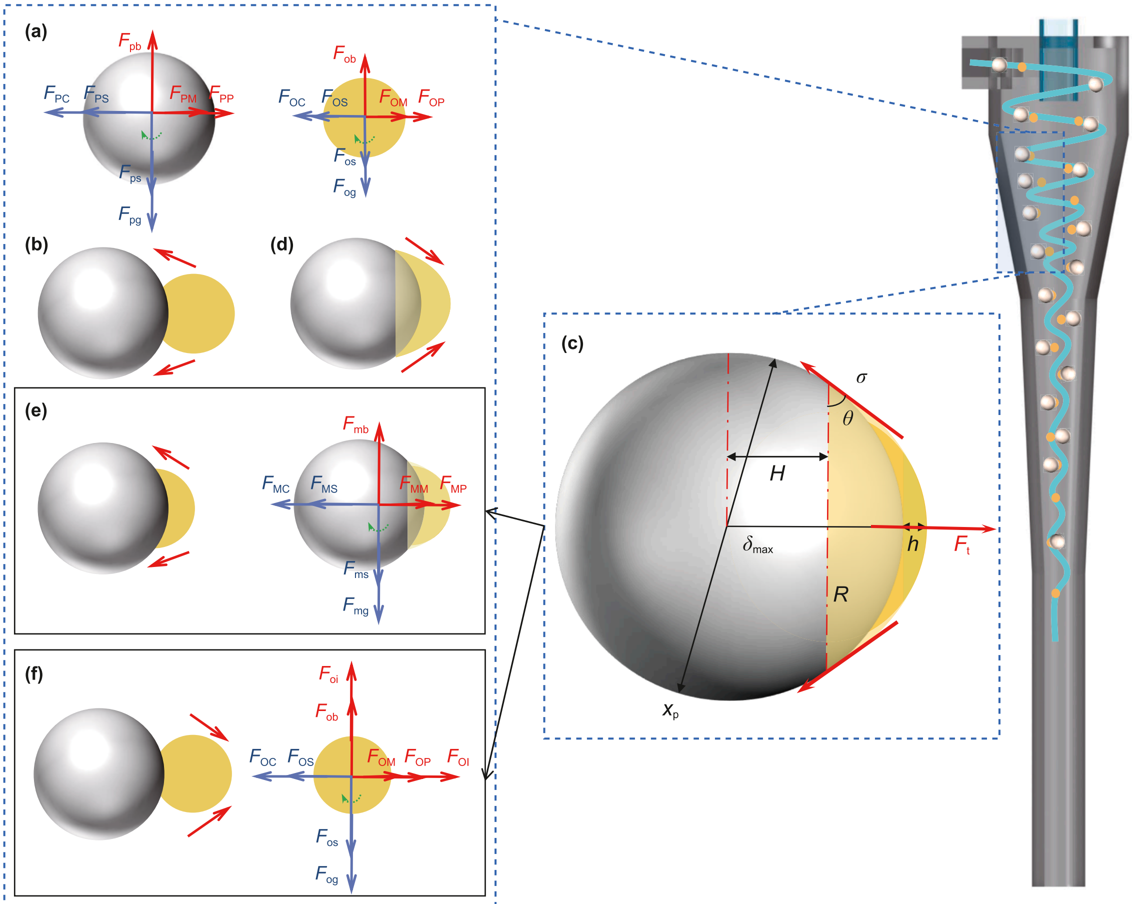

Fig. 7. Coupled separation process of particles and oil droplets.

spreading angle $2\delta_{max}$. At the maximum spreading state, the corresponding solid–liquid interfacial energy E_{op} can be expressed as:

$$E_{op} = A_{op}\sigma_{op} = 2\pi \times \frac{x_p}{2} \times \left(\frac{x_p}{2} - H\right)\sigma_{op} = \pi\sigma_{op}x_p\left(\frac{x_p}{2} - H\right) \tag{15}$$

where A_{op} is the contact area between the oil droplet and the particle, and σ_{op} represents the interfacial tension between the oil droplet and the particle.

The potential energy of the solid–liquid interface at the maximum spreading state E_{pp} can be expressed as:

$$E_{pp} = m_o g h_l = m_o g(x_p + h)\frac{1 + \cos\delta'_{max}}{4} \tag{16}$$

where h_l is the height of the centroid of the oil film, δ'_{max} denotes the maximum spreading angle, and δ_{max} represents its corresponding value in radians.

The viscous dissipation energy E_{vd} is typically concentrated within the boundary layer near the solid surface and can be expressed as:

$$E_{vd} = \frac{\sqrt{Re}\mu v \pi x_p^2(1 - \cos\delta'_{max})c_{max}}{4x_o} \tag{17}$$

where μ denotes the dynamic viscosity of the droplet, v is the instantaneous velocity of the droplet, and c_{max} is the maximum arc length of the central cross-section of the oil droplet–particle contact surface, which can be expressed as $c_{max} = \delta_{max}x_p$.

During the spreading process, as shown in Fig. 7(b), the kinetic energy of the oil droplet is progressively converted into surface energy and viscous dissipation. Inertial forces promote spreading, while surface tension and viscous forces resist it, leading to a gradual decrease in spreading velocity until the maximum spreading diameter is reached, as indicated in Fig. 7(c). At this point, the droplet's kinetic energy approaches zero, and surface energy is maximized. To characterize the dominant force during spreading, Clanet et al. proposed a dimensionless parameter P (Clanet et al., 2004):

$$P = \frac{We}{Re^{4/5}} \tag{18}$$

where, We is the Weber number (the ratio of inertial to surface tension forces), and Re is the Reynolds number (the ratio of inertial to viscous forces). When $P < 0.3$, surface tension dominates, resulting in rapid deceleration of spreading; when $P > 0.3$, viscous forces dominate.

After reaching maximum spreading, the droplet undergoes a retraction process, as shown in Fig. 7(d). The main driving forces during retraction are the liquid-liquid interfacial tension and the tensile force exerted by the flow field, while the primary resistance is the adhesive force at the solid-liquid interface. If the tensile force from the flow field (F_t) is smaller than the interfacial

Petroleum Science 23 (2026) 5174–5188

adhesion force, the droplet remains stably attached to the particle surface.

$$F_t < 2\pi R\sigma \cdot \sin\alpha \tag{19}$$

where, σ represents the interfacial tension between the oil droplet and the particle, and α is the contact angle of the oil droplet on the particle surface.

In the radial direction of the hydrocyclone field, the resultant force primarily responsible for separating oil droplets from particle surfaces can be expressed as:

$$F_t = F_P - F_C \tag{20}$$

where, F_t, F_P and F_C denote the tensile force exerted by the flow field, the pressure gradient force, and the centrifugal force, respectively. The expressions for F_C and F_P are given as:

$$F_C = \rho_o V \frac{v^2}{r_o} \tag{21}$$

$$F_P = \rho_w V \frac{v^2}{r_o} \tag{22}$$

where, ρ_o is the oil droplet density, ρ_w is the water density, and r_o is the rotation radius (i.e., the radial distance from the hydrocyclone axis), V is the volume of the spherical cap formed at the droplet's maximum spreading state, can be expressed as:

$$V = \frac{1}{3}\pi\left(R - x_p \cdot \cos\alpha\right)^2 \cdot \left(2R + x_p \cdot \cos\alpha\right)^2 \tag{23}$$

Combining Eqs. (19)–(23), the critical condition for the interfacial stability of the oil droplet on the particle surface in the hydrocyclone can be further derived as:

$$(\rho_w - \rho_o) \cdot \frac{1}{3}\pi\left(R - x_p \cdot \cos\alpha\right)^2 \cdot \left(2R + x_p \cdot \cos\alpha\right)^2 \cdot \frac{v^2}{r_o} < 2\pi R\sigma \cdot \sin\alpha \tag{24}$$

$$v < \sqrt{\frac{6 r_o R\sigma \cdot \sin\alpha}{(\rho_w - \rho_o)\left(R - x_p \cdot \cos\alpha\right)^2 \left(2R + x_p \cdot \cos\alpha\right)^2}} \tag{25}$$

According to Eq. (25), the interfacial stability between the oil droplet and the particle in a hydrocyclone is mainly influenced by several factors, including the flow velocity, particle diameter, oil droplet diameter and spreading radius, oil density, and the contact angle at the solid–liquid interface. In addition, shear stress in tangential direction also plays a significant role, which is largely governed by the local flow velocity.

Under the above conditions, when the particle radius is small, the radial distance from the hydrocyclone axis is large, and the contact angle between the solid and liquid phases is low (i.e., the solid surface exhibits good wettability toward the oil phase), the oil droplet is more likely to stably spread and adhere to the particle surface, as shown in Fig. 7(e). In this case, an oil droplet–particle complex is formed, resulting in a greater centrifugal force difference between the complex and the surrounding water phase within the hydrocyclone field. This enhances the tendency of the complex to migrate toward the axis, thereby promoting the effective separation of fine oil droplets.

Conversely, when the wettability between the particle and the oil droplet is poor or the collision conditions are unfavorable, the oil droplet is more likely to rebound, as illustrated in Fig. 7(f). In this scenario, the rebounding oil droplet is subjected to a thrust exerted by the particle, causing it to move further toward the axis. Although this also facilitates its detachment from the water phase, the enhancement effect may be less significant than that achieved through stable adhesion.

3.2. Experimental results and analysis

3.2.1. Oil droplet-particle and droplet-droplet coalescence behaviors

Key frames were extracted from high-speed camera recordings to analyze the collision and coalescence behaviors between oil droplets and particles, as well as between oil droplet–particle complexes and oil nuclei. These frames capture the main morphological features and deformation dynamics during the coalescence process. In this analysis, Δt represents the time interval. As shown in Fig. 8, after entering the swirling flow field, an oil droplet collides with an oil nucleus, resulting in pronounced elongation and deformation. The deformed droplet subsequently undergoes rotational motion and entwines with the oil nucleus, leading to coalescence. The images reveal that in the absence of particles, discrete oil droplets in the swirling flow field experience continuous oscillatory deformation. At Δt = 0.05 s, significant coalescence is observed, followed by continued deformation and upward merging at Δt = 0.18 s. After Δt = 0.4 s, the oil nucleus remains largely unchanged.

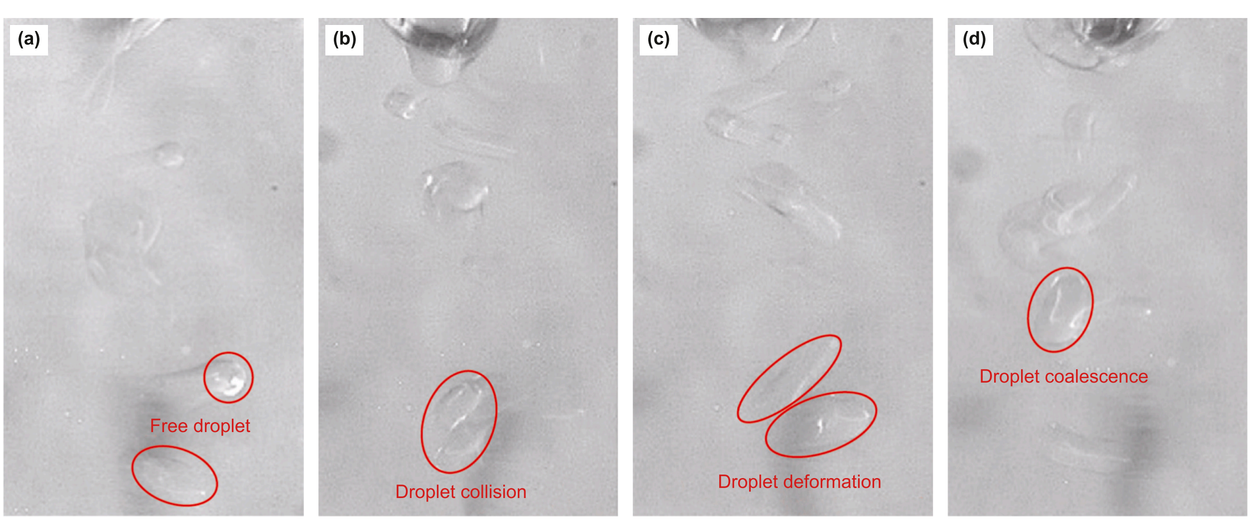

Fig. 8. Morphological evolution and deformation of oil droplet aggregation. (**a**) Δt = 0 s; (**b**) Δt = 0.05 s; (**c**) Δt = 0.18 s; (**d**) Δt = 0.4 s.

Fig. 9 shows the state of oil nuclei after particles injection into the swirling flow field, where particles are encapsulated by oil droplets. Compared with Fig. 8, although oil droplet coalescence is still evident, a small number of droplets remain free or detached from the nucleus. In contrast, with particle addition, oil droplets rapidly combine with particles to form oil droplet–particle complexes. These complexes migrate upward and continuously adsorb surrounding droplets, promoting further coalescence and the formation of larger agglomerates. Compared to the system without particles, the complexes move more centrally and show fewer detached droplets at the same time intervals. This demonstrates that introducing suitable particles enhances the centripetal transport of oil droplets, thereby improving the separation efficiency in the swirling flow field.

3.2.2. *Morphological evolution of droplet–particle complexes at varying rotational speeds*

Theoretical analysis suggests that flow velocity significantly influences the post-collision behavior between oil droplets and oleophilic particles in a coupled swirling flow field. Therefore, a comparative analysis was conducted to observe the evolution of droplet–particle complexes under different rotational speeds. Fig. 10 illustrates the dynamic morphological changes of complexes at a low rotational speed of 800 r/min.

In the initial state, both oil droplets and droplet–particle complexes were observed in the swirling flow field. At Δt = 1.33 s, noticeable deformation occurred in the free oil droplets, while the morphology of the complexes remained nearly unchanged. This indicates that the shear stress in the flow field has a limited impact on deforming solid–liquid interfaces but significantly affects free droplets. At Δt = 2.13 s, some complexes in the lower region began to migrate upward and aggregate. Meanwhile, small oil droplets not coupled with particles were also observed, likely due to insufficient centrifugal force differentials at low rotational speeds. By Δt = 4.57 s, significant aggregation of the complexes occurred, further confirming that, compared to free droplets, the complexes—having lower density and larger size—are more prone to be separated.

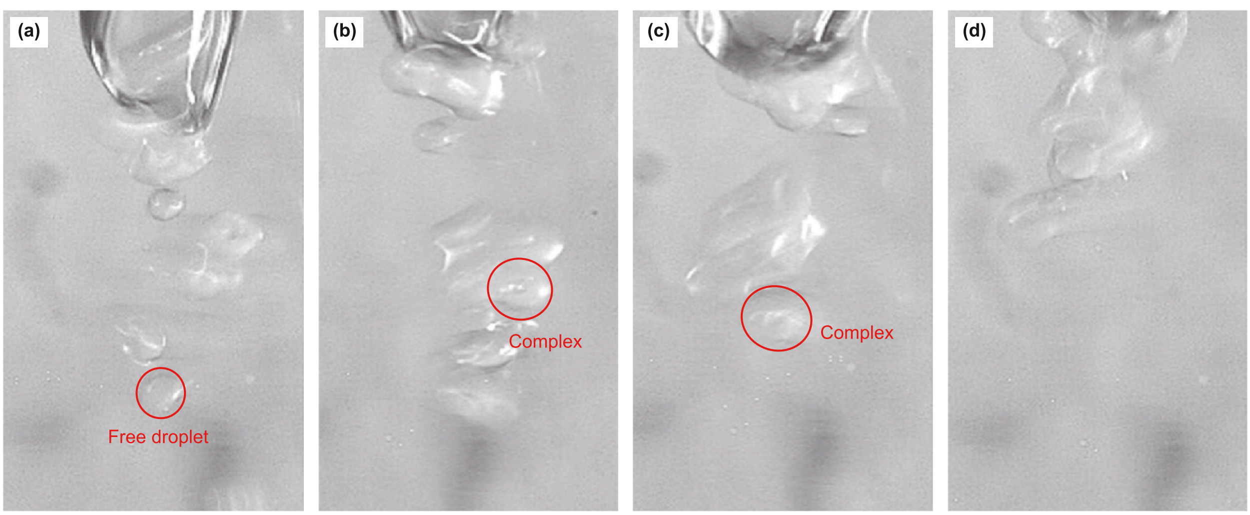

Fig. 9. Coupling and aggregation of oil droplets and particles. (**a**) Δt = 0 s; (**b**) Δt = 0.05 s; (**c**) Δt = 0.18 s; (**d**) Δt = 0.4 s.

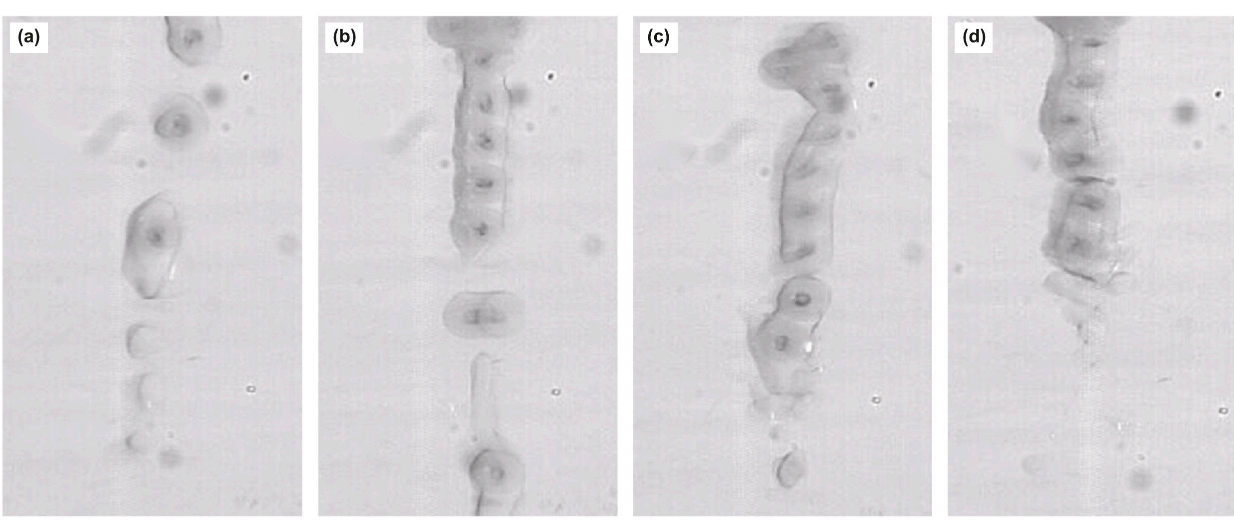

Fig. 10. Morphological evolution of droplet–particle complexes at a rotational speed of 800 r/min. (**a**) Δt = 0 s; (**b**) Δt = 1.33 s; (**c**) Δt = 2.13 s; (**d**) Δt = 4.57 s.

Fig. 11 presents the dynamic evolution of the complexes at a medium rotational speed of 1000 r/min. Initially, most oil droplets were already attached to particles, forming multiple complexes, although a few free droplets were still present. At $\Delta t = 1.033$ s, nearly all oil droplets had coalesced with particles. At $\Delta t = 1.983$ s, these complexes continued to adsorb surrounding droplets and migrate upward. By $\Delta t = 3.367$ s, coalescence between different complexes occurred, leading to the formation of larger aggregates that moved collectively toward the upper region. These observations indicate that a moderate increase in flow velocity promotes more effective coalescence between droplets and particles.

Fig. 12 presents the dynamic evolution of complexes at a higher rotational speed of 1200 r/min. Initially, most oil droplets had already coalesced with particles, and aggregation between complexes was also observed. At $\Delta t = 0.417$ s, droplet–particle separation occurred, forming detached droplets, indicating that the drag force exceeded the interfacial adhesion at that moment. At $\Delta t = 0.834$ s, more droplets detached from particle surfaces under intensified centrifugal forces, resulting in numerous free droplets in the flow field. By $\Delta t = 2.4$ s, frequent events of coalescence, separation, and rebound between droplets and particles were observed.

Comparative analysis of Figs. 10–12 reveals a significant difference in the morphological evolution of droplet–particle interactions at various rotational speeds. At low speeds, stable complexes were formed, and their structure remained largely unchanged over time, with minimal droplet detachment. At medium speeds, coalescence and aggregation between complexes were more pronounced. In contrast, at high speeds, many oil droplets rebounded or separated from the particles shortly after collision (e.g., $\Delta t = 0.417$ s), forming detached droplets. These findings are crucial for understanding the interaction dynamics between oil droplets and particles in complex flow environments and further confirm the existence of speed-dependent critical conditions governing their post-collision behavior.

3.3. Numerical simulation results and analysis

To further evaluate the effectiveness of oleophilic particle-enhanced hydrocyclones and verify the accuracy of the viscous force model, a comparative analysis was conducted under operating conditions with an inlet flow rate of 2.4 m^3/h and a split ratio of 20%. The study compared the flow field characteristics and separation performance of a conventional hydrocyclone (CHC),

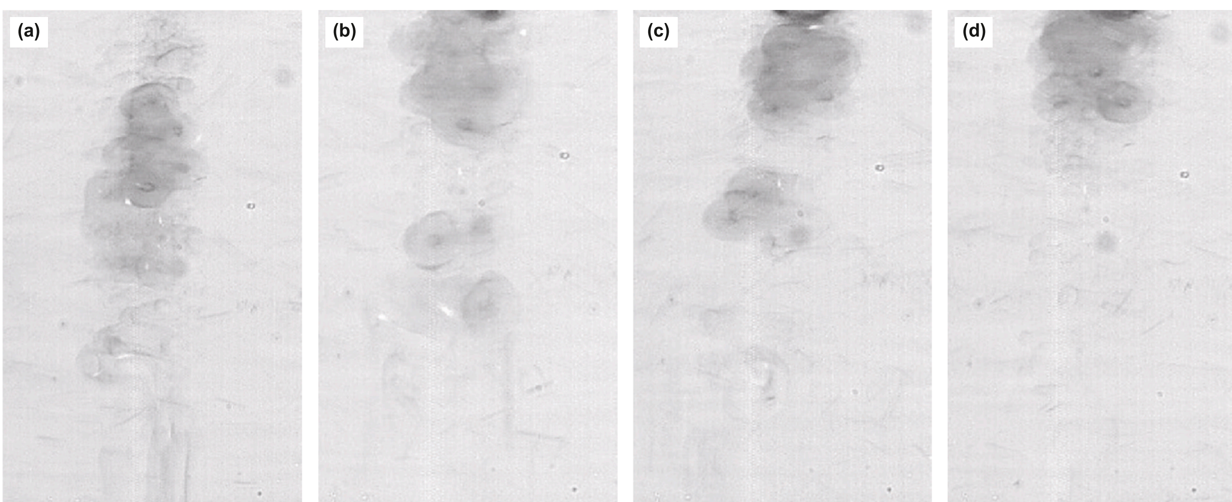

Fig. 11. Morphological evolution of droplet–particle complexes at a rotational speed of 1000 r/min. (**a**) $\Delta t = 0$ s; (**b**) $\Delta t = 1.033$ s; (**c**) $\Delta t = 1.983$ s; (**d**) $\Delta t = 3.367$ s.

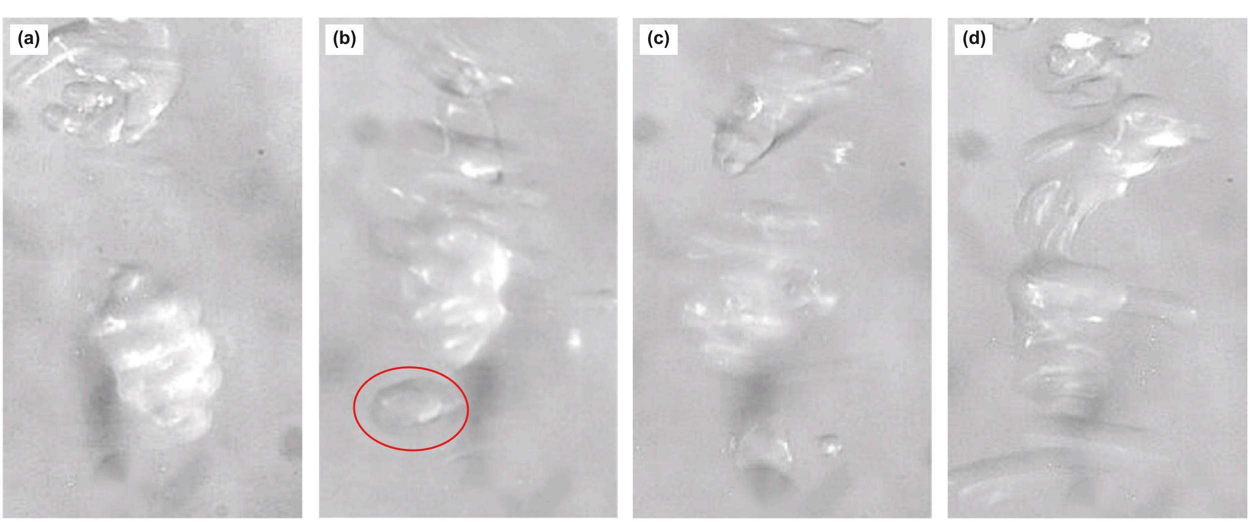

Fig. 12. Morphological evolution of droplet–particle complexes at a rotational speed of 1200 r/min. (**a**) $\Delta t = 0$ s; (**b**) $\Delta t = 0.417$ s; (**c**) $\Delta t = 0.834$ s; (**d**) $\Delta t = 2.4$ s.

hydrocyclones coupled with particles of different properties (HCCP-1 and HCCP-2), and a hydrocyclone coupled with oleophilic particles (HCCOP). In HCCP-1, the particle density and diameter were 890 kg/m^3 and 300 μm, respectively, while in HCCP-2, the particle density and diameter were 905 kg/m^3 and 355 μm, respectively.

3.3.1. Coupling interactions between particles and flow field

Fig. 13 illustrates the effect of particles on the velocity distribution in the flow field, where oil droplets of different diameters are distinguished by color and size, and particles are shown in gray. The background contour indicates the velocity magnitude, revealing the flow-field variation under different coupling conditions. As shown in Fig. 13(a) and (b), compared to CHC, the flow velocity in HCCP shows a moderate increase, especially near the inner vortex region. This suggests that particles not only assist in driving the motion of oil droplets but also enhance the movement of the surrounding fluid, which in turn further promotes oil droplet transport. Additionally, the upper section of the large cone, where particles are densely concentrated, shows slightly higher velocities than the middle section, where particle density is lower. This further demonstrates the coupling effect between particles and the fluid flow. The increased velocity in the lower cone section is primarily due to the narrowing of the flow area. A comparison between Fig. 13(c) and (d) also reveals a significant reduction in the number of oil droplets near the hydrocyclone wall, indicating that oleophilic particles exhibit an enhanced carrying effect on oil droplets.

Tangential velocity is the dominant velocity component in a hydrocyclone. To further analyze particle-flow coupling, velocity profiles were extracted along three lines (Line 1, Line 2, and Line 3) located at the upper, middle, and lower regions of the large cone section, As shown in Fig. 14. In Fig. 14(a) and (b), HCCOP exhibits higher tangential velocity than HCCP-2 in the upper and middle axial regions, primarily due to the continuous agglomeration between oleophilic particles and oil droplets, which enhances momentum transfer to the surrounding fluid. In contrast, as shown in Fig. 14(c), near the wall and in the lower cone section, HCCOP shows lower tangential velocity than HCCP-2, which is also related to particle motion. Due to the strong adsorption of oil droplets by oleophilic particles, the number of droplets and particles in these regions is significantly reduced, as shown in Fig. 13(d), thereby diminishing their influence on the surrounding flow.

3.3.2. Coupling interaction between particles and oil droplets

The average contact force between particles and oil droplets over time is illustrated in Fig. 15. As shown, in the HCCP systems, particles with lower density and larger size exhibit stronger average contact forces with oil droplets. Specifically, the maximum average contact force increased from 3.12 × 10^{-5} N in HCCP-1 to 4.21 × 10^{-5} N in HCCP-2, indicating that the particles exert a stronger pushing effect on the droplets. Further comparison with

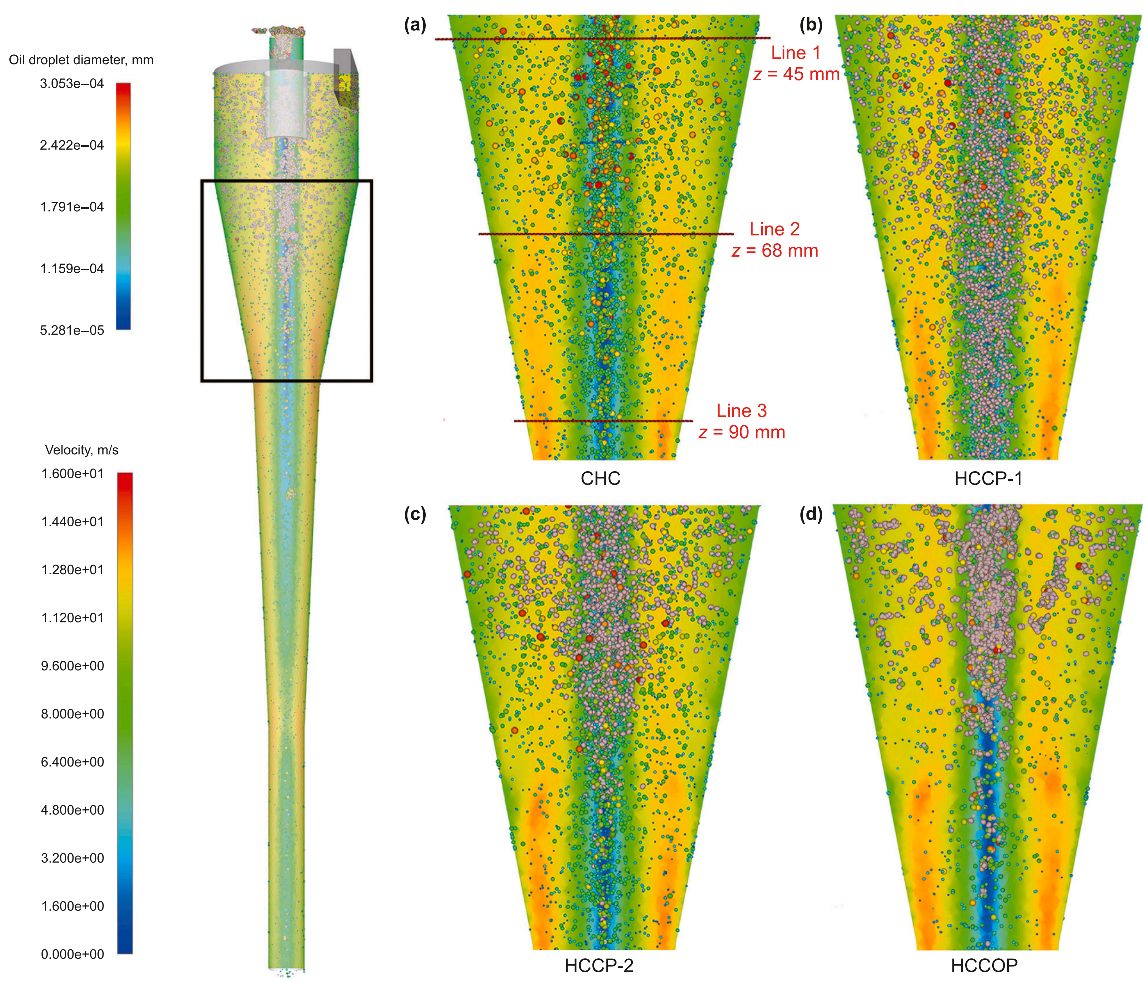

Fig. 13. The impact of particles on flow field velocity distribution.

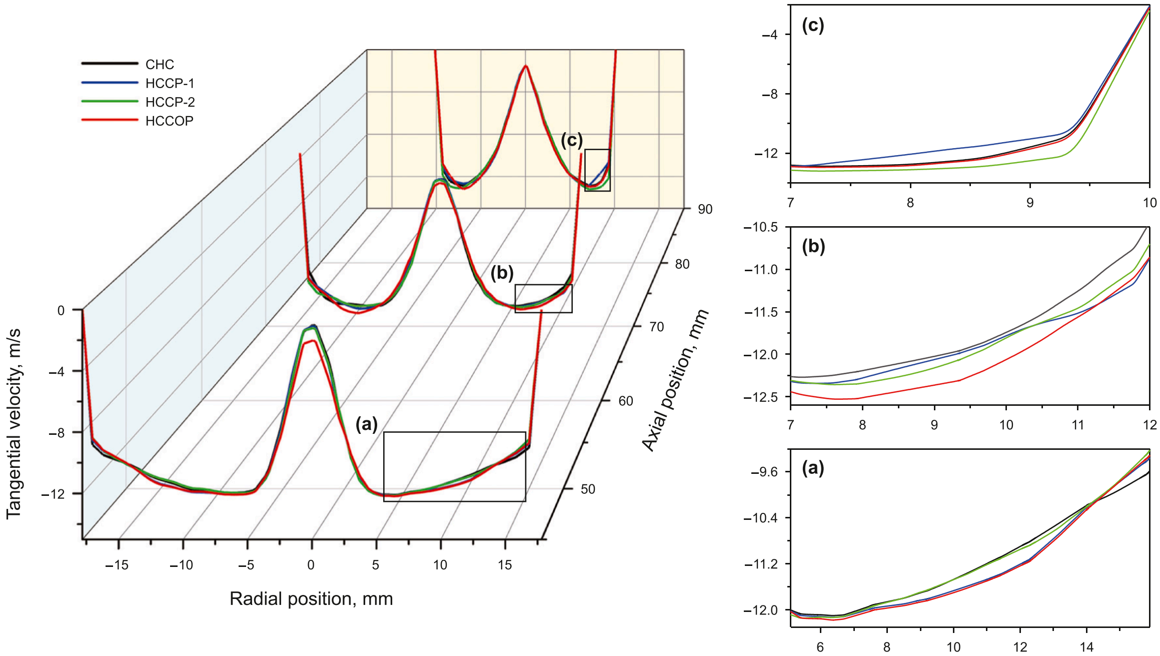

Fig. 14. The impact of particles on tangential velocity. (**a**) Line 1; (**b**) line 2; (**c**) line 3.

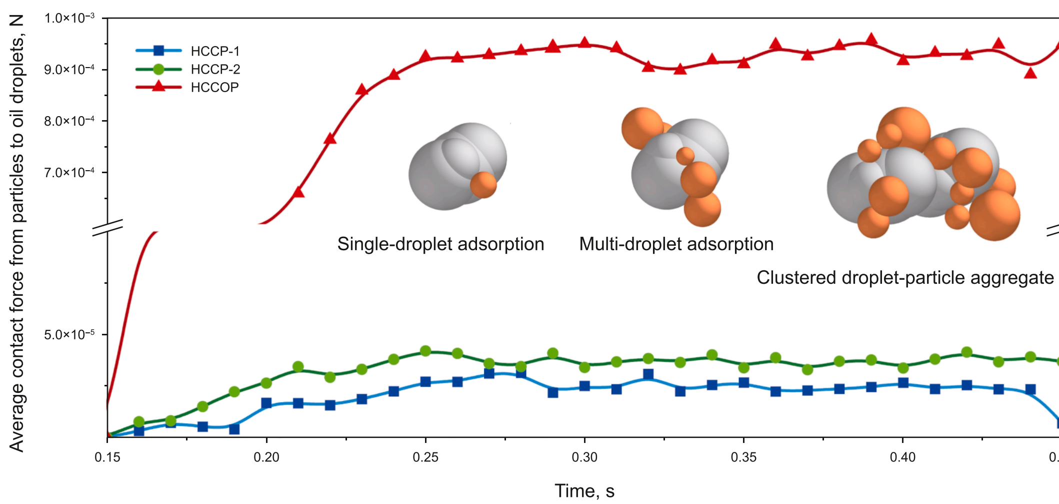

Fig. 15. Variation of average combined contact force over time between particles and oil droplets.

HCCOP reveals that the contact force between particles and oil droplets increases significantly, with the peak average contact force reaching 9.48×10^{-4} N. This enhancement is primarily due to the fact that, in HCCP-1 and HCCP-2, the contact force is mainly the mechanical pushing force from particles. In contrast, in HCCOP, the contact force includes not only the pushing force but also the adhesive force arising from the calibrated JKR surface energy between oleophilic particles and oil droplets. Fig. 15 demonstrates that, in the particle-coupled hydrocyclone process, the adsorption effect between oleophilic particles and oil droplets is particularly significant, which further enhances the coupling interaction between them.

To further investigate the coupling effect of particles on oil droplets, the distribution of the dispersed-phase oil droplets and particles in HCCP systems was analyzed, as shown in Fig. 16. A comparison between Fig. 16(a) and (b) indicates that, after optimizing particle properties, the dispersed phase becomes more concentrated in the coupled field, particularly near the hydrocyclone axis (HCCP-2 compared to HCCP-1). However, in HCCP-2, a portion of the dispersed phase is still discharged through the underflow outlet, suggesting that relying solely on the pushing effect of particles on oil droplets has limitations in enhancing separation performance. Fig. 16(c) shows that in HCCOP, the concentration of the dispersed phase further increases near the axis, while the concentration at the underflow decreases. This observation confirms the significant adsorption effect between oleophilic particles and oil droplets in the particle-coupled hydrocyclone system. The continuous aggregation between oleophilic particles and oil droplets leads to an increase in the size and a decrease in the density of the droplet–particle complexes, making them more likely to migrate toward the overflow outlet. This reveals the crucial role of particle adsorption in improving hydrocyclone separation efficiency. In summary, both the collision-induced pushing effect and the adsorption-carrying

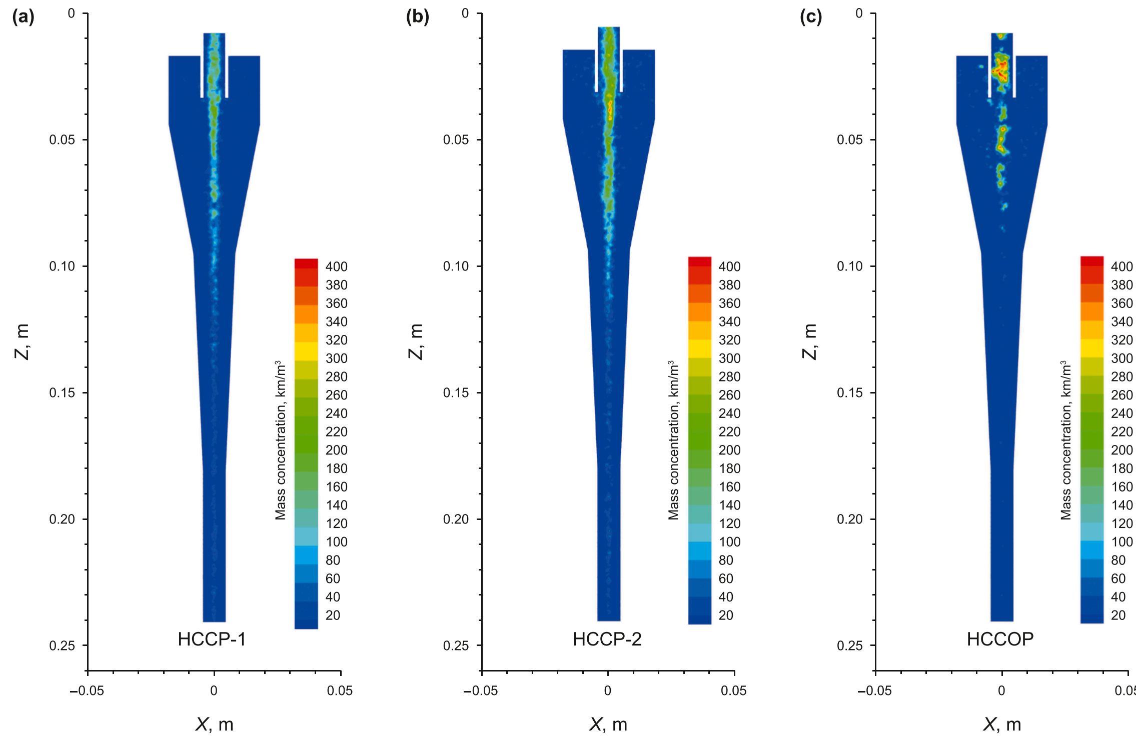

Fig. 16. Discrete phase concentration distribution within HCCP.

effect of particles on oil droplets significantly contribute to the enhanced performance of the HCCP system.

3.3.3. Comparison of separation efficiency

Fig. 17 presents a comparison of the overall separation efficiency among CHC, HCCP-1, HCCP-2, and HCCOP. The results demonstrate that HCCOP exhibits a significant advantage, improving separation efficiency by 8.19 percentage points compared to CHC. Furthermore, Fig. 18 compares the grade separation efficiency for oil droplets of different diameters. It can be observed that when the droplet diameter is smaller than 250 μm, the coupled separation approach significantly improves grade efficiency. In particular, for droplets smaller than 150 μm, the use of oleophilic particles enhances the separation efficiency by approximately 9.6%—29.68%. Specifically, for droplets with a diameter of 67 μm, the separation efficiency increases by up to 29.68 percentage points, reaching 79.23%. Meanwhile, compared with CHC, the pressure drop of HCCOP increased by only 0.012 MPa. This indicates that the coupling of oleophilic particles significantly enhances the oil-water separation performance without introducing additional energy consumption.

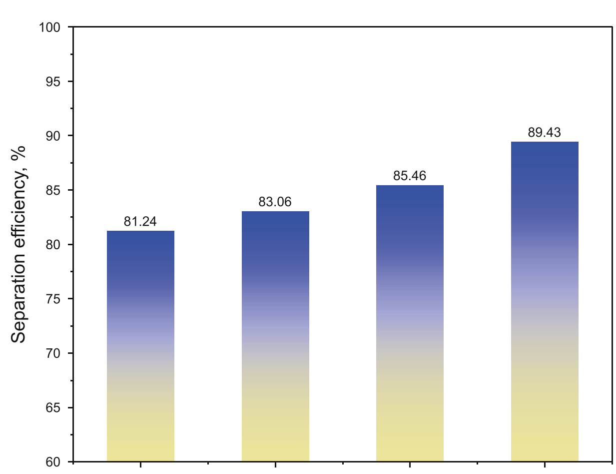

Fig. 17. Comparison of separation efficiency.

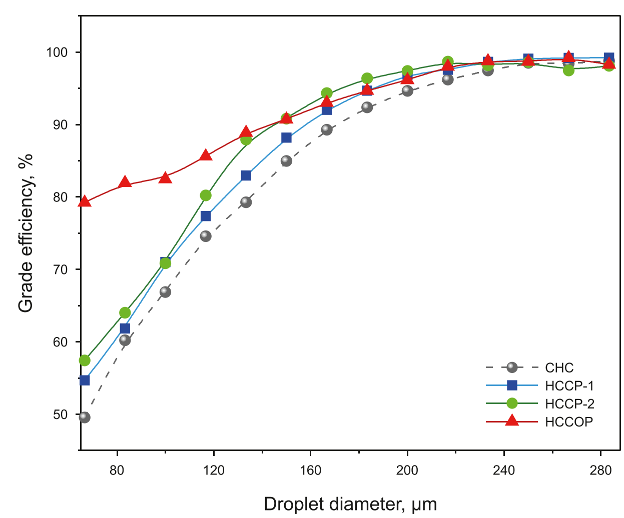

Fig. 18. Comparison of grade efficiency.

These findings are consistent with previous experimental studies (Zhang et al., 2023). In addition, for the separation of fine oil droplets, Liu et al. proposed using mini-hydrocyclones to improve separation performance. However, their results showed that mini-hydrocyclones achieved less than 65% efficiency for 100 μm oil droplets (Liu et al., 2019), whereas HCCOP proposed in this study achieved a significantly higher efficiency. The superior separation of fine droplets in the HCCOP system results from the combined effects of particle-driven propulsion and interfacial adsorption, which accelerate droplet migration toward the hydrocyclone axis. These results demonstrate the strong potential and practical advantages of particle-coupled hydrocyclone systems for enhancing oil–water separation efficiency, particularly for fine-droplet treatment.

4. Conclusions

This study integrates theoretical derivation, visualization experiments, and numerical simulations to systematically elucidate the mechanism by which hydrocyclones coupled with particles enhance oil–water separation. A critical judgment model for oil droplet–particle collisions was established, and a multiphase coupling simulation model was developed based on the Johnson–Kendall–Roberts (JKR) adhesion theory. The key role of oleophilic particles in promoting oil droplet coalescence and separation was validated. This study provides theoretical support and data evidence for optimizing and applying hydrocyclones coupled with particles. The main conclusions are as follows.

(1) Theoretical analysis identified the critical conditions governing oil droplet–particle interactions after collision and clarified the key factors affecting stable adsorption. Smaller particle diameter, larger radial position, and smaller contact angle increase the critical rebound velocity, thereby enhancing droplet-particle adhesion.
(2) Visualization experiments demonstrated that particles effectively promote the migration of oil droplets toward the center of the hydrocyclone field. At lower rotational speeds, droplet–particle collisions primarily form stable complexes, whereas at higher rotational speeds, collisions are more likely to result in rebound and re-separation.
(3) A discrete element model was developed to characterize particle–oil droplet adsorption in the hydrocyclone field. The model was validated by comparing simulated and measured angles of repose, with a deviation of only 0.24%, confirming the reliability of the JKR adhesion model.
(4) Numerical simulations show that oleophilic particles significantly enhance droplet adhesion and improve overall separation efficiency by 8.19 percentage points. For 67 μm oil droplets, HCCOP achieves 79.23% separation efficiency—29.68 percentage points higher than CHC—highlighting its strong adhesion and separation advantages.

CRediT authorship contribution statement

Shuang Zhang: Writing – original draft, Software, Methodology, Formal analysis, Conceptualization. **Li-Xin Zhao:** Writing – review & editing, Supervision, Resources, Conceptualization. **Xing-Yue Chen:** Software, Investigation. **Lin Liu:** Validation, Software. **Ming-Hu Jiang:** Writing – review & editing, Methodology.

Declaration of competing interest

The authors declare that they have no known competing financial interests or personal relationships that could have appeared to influence the work reported in this paper.

Acknowledgements

This work was supported by the National Key Research and Development Program of China (Grant No. 2024YFE0213100), the Joint Funds of the National Natural Science Foundation of China (Key program) (Grant No. U21A20104), and the Northeast Petroleum University "National Fund" Incubation Fund, China (Grant No. 2024GPL-06).

References

Amakiri, K.T., Canon, A.R., Molinari, M., Angelis-Dimakis, A., 2022. Review of oilfield produced water treatment technologies. Chemosphere 298, 134064. https://doi.org/10.1016/j.chemosphere.2022.134064.
Bhamjee, M., Connell, S.H., Nel, A.L., 2022. The modification of the dynamic behaviour of the cyclonic flow in a hydrocyclone under surging conditions. Math. Comput. Appl. 27 (6), 88. https://doi.org/10.3390/mca27060088.
Bordbar, A., Taassob, A., Khojasteh, D., Marengo, M., Kamali, R., 2018. Maximum spreading and rebound of a droplet impacting onto a spherical surface at low weber numbers. Langmuir 34 (17), 5149–5158. https://doi.org/10.1021/acs.langmuir.8b00625.
César, S.D., De Jager, D., Njoya, M., 2025. The role of hydrocyclone and induced gas flotation technologies in offshore produced water deoiling advancements. Pet. Res. 10 (2), 342–351. https://doi.org/10.1016/j.ptlrs.2024.10.002.
Chen, J., Wang, Q., Xiao, J., An, S., Hao, J., Zhang, M., Wang, X., Luan, Z., Ji, Y., 2020. Development status and prospect of water pre-separation technology for produced liquid in high water-cut oil well. Acta Pet. Sin. 41 (11), 1434. https://doi.org/10.7623/syxb202011013 (in Chinese).
Clanet, C., Béguin, C., Richard, D., Quéré, D., 2004. Maximal deformation of an impacting drop. J. Fluid Mech. 517, 199–208. https://doi.org/10.1017/s0022112004000904.
Cunha, R.N., Santos, K.G., Lima, R.N., Duarte, C.R., Barrozo, M.A.S., 2016. Repose angle of monoparticles and binary mixture: an experimental and simulation study. Powder Technol. 303, 203–211. https://doi.org/10.1016/j.powtec.2016.09.023.
Dai, Y., Yang, X., Du, J., Yu, W., Wang, D., Yuan, F., 2025. Migration and removal of microplastics in a dual-cone mini-hydrocyclone. Symmetry 17 (9), 1559. https://doi.org/10.3390/sym17091559.
Dalgamoni, H.N., Yong, X., 2021. Numerical and theoretical modeling of droplet impact on spherical surfaces. Phys. Fluids 33 (5). https://doi.org/10.1063/5.0047024.
Deng, X., Scicolone, J.V., Davé, R.N., 2013. Discrete element method simulation of cohesive particles mixing under magnetically assisted impaction. Powder Technol. 243, 96–109. https://doi.org/10.1016/j.powtec.2013.03.043.
E, D., Hu, H., Ye, Q., Zhou, Z., Zou, R., Yu, A., Kuang, S., 2025. Multi-objective optimization of hydrocyclones inlet configurations for improving separation performance. Powder Technol. 456, 120772. https://doi.org/10.1016/j.powtec.2025.120772.
Ekechukwu, O.M., Asim, T., Hawez, H.K., 2024. Recent developments in hydrocyclone technology for oil-in-water separation from produced water. Energies 17 (13), 3181. https://doi.org/10.3390/en17133181.
Fan, Z., Liu, D., Pan, S., Ma, J., Chen, X., 2023. Spreading dynamics of the viscous droplet impacting on a spherical particle. Phys. Fluids 35 (2). https://doi.org/10.1063/5.0137718.
Fatahian, H., Fatahian, E., Nimvari, M.E., Ahmadi, G., 2021. Novel designs for square cyclone using rounded corner and double-inverted cones shapes. Powder Technol. 380, 67–79. https://doi.org/10.1016/j.powtec.2020.11.034.
Fu, P., Huang, Y., Wang, J., Fan, Y., Lyu, W., Huang, C., Yang, Q., Wei, Y., Wang, H., 2020. Process intensification technology for hydrocyclone separation. Chem. Ind. Eng. Prog. 39 (12), 4766. https://doi.org/10.16085/j.issn.1000-6613.2020-1011.
Gao, Y., 2018. Quantitative simulation on powder shear flow using discrete element method. J. Pharm. Innov. 13 (4), 330–340. https://doi.org/10.1007/s12247-018-9324-2.
Gao, Z.W., Liu, Z.X., Wei, Y.D., Li, C.X., Wang, S.H., Qi, X.Y., Huang, W., 2022. Numerical analysis on the influence of vortex motion in a reverse Stairmand cyclone separator by using LES model. Pet. Sci. 19 (2), 848–860. https://doi.org/10.1016/j.petsci.2021.11.009.
Han, D.D., Xu, Y., Huang, Y.X., He, B., Dai, J.W., Lv, X.R., Zhang, L.H., 2023. DEM parameters calibration and verification for coated maize particles. Comput. Part. Mech. 10 (6), 1931–1941. https://doi.org/10.1007/s40571-023-00598-7.
Hou, D., Zhao, Q., Cui, B., Wei, D., Song, Z., Feng, Y., 2022. Geometrical configuration of hydrocyclone for improving the separation performance. Adv. Powder Technol. 33 (2), 103419. https://doi.org/10.1016/j.apt.2021.103419.
Kharoua, N., Khezzar, L., Nemouchi, Z., 2010. Hydrocyclones for de-oiling applications—A review. Petrol. Sci. Technol. 28 (7), 738–755. https://doi.org/10.1080/10916460902804721.
Li, X., Du, Y., Liu, L., Zhang, Y., Guo, D., 2022. Parameter calibration of corncob based on DEM. Adv. Powder Technol. 33 (8), 103699. https://doi.org/10.1016/j.apt.2022.103699.
Liu, H., Gao, Y., Pei, X., Zheng, G., Zheng, L., 2018. Progress and prospect of downhole cyclone oil-water separation with single-well injection-production technology. Acta Petrol. Sin. 39 (4), 463. https://doi.org/10.7623/syxb201804010.
Liu, L., Zhao, L., Wang, Y., Zhang, S., Song, M., Huang, X., Lu, Z., 2022. Research on the enhancement of the separation efficiency for discrete phases based on mini hydrocyclone. J. Mar. Sci. Eng. 10 (11), 1606. https://doi.org/10.3390/jmse10111606.

Liu, L., Zhao, L., Yang, X., Wang, Y., Xu, B., Liang, B., 2019. Innovative design and study of an oil-water coupling separation magnetic hydrocyclone. Sep. Purif. Technol. 213, 389–400. https://doi.org/10.1016/j.seppur.2018.12.051.
Liu, P., Chen, B., Hou, D., Jiang, Z., Yan, Z., Han, Z., 2024a. Study on the separation performance of a two cylindrical section hydrocyclone under various height ratios. ACS Omega 9 (19), 21569–21579. https://doi.org/10.1021/acsomega.4c02365.
Liu, Q., Liu, S., Li, Y., Liu, Y., Wang, N., Yang, Q., Lu, H., 2024b. Microbubble-based process for the enhancement of microfine and heavy oil droplets swirl separation in axial inlet hydrocyclone. Sep. Purif. Technol. 332, 125642. https://doi.org/10.1016/j.seppur.2023.125642.
Lupo, M., Barletta, D., Sofia, D., Poletto, M., 2021. Calibration of DEM for cohesive particles in the SLS powder spreading process. Processes 9 (10), 1715. https://doi.org/10.3390/pr9101715.
Lu, M., Zhao, L., Peng, Z., Zhang, S., Jiang, M., 2024. Research progress on the influence of structural and operating parameters on the enhanced separation performance of mini-hydrocyclones. Chem. Eng. Res. Des. 208, 81–93. https://doi.org/10.1016/j.cherd.2024.06.045.
Mahmud, T., Haque, J.N., Roberts, K.J., Rhodes, D., Wilkinson, D., 2009. Measurements and modelling of free-surface turbulent flows induced by a magnetic stirrer in an unbaffled stirred tank reactor. Chem. Eng. Sci. 64 (20), 4197–4209. https://doi.org/10.1016/j.ces.2009.06.059.
Malgarinos, I., Nikolopoulos, N., Gavaises, M., 2016. A numerical study on droplet-particle collision dynamics. Int. J. Heat Fluid Flow 61, 499–509. https://doi.org/10.1016/j.ijheatfluidflow.2016.06.010.
Mitra, S., Evans, G.M., Doroodchi, E., Pareek, V., Joshi, J.B., 2017. Interactions in droplet and particle system of near unity size ratio. Chem. Eng. Sci. 170, 154–175. https://doi.org/10.1016/j.ces.2017.03.059.
Patel, M., Patel, J., Pawar, Y., Patel, N., Shah, M., 2020. Membrane-based downhole oil–water separation (DOWS) technology: an alternative to hydrocyclone-based DOWS. J. Pet. Explor. Prod. Technol. 10 (5), 2079–2088. https://doi.org/10.1007/s13202-020-00848-x.
Pukkella, A.K., Vega-Garcia, D., Hadler, K., Cilliers, J., 2025. The influence of surface-wall roughness on hydrocyclone performance. Sep. Purif. Technol. 360, 131109. https://doi.org/10.1016/j.seppur.2024.131109.
Shahzad, K., Aeken, W.V., Mottaghi, M., Kamyab, V.K., Kuhn, S., 2018. Aggregation and clogging phenomena of rigid microparticles in microfluidics: Comparison of a discrete element method (DEM) and CFD–DEM coupling method. Microfluid. Nanofluidics 22 (9), 104. https://doi.org/10.1007/s10404-018-2124-7.
Tian, J., Ni, L., Song, T., Olson, J., Zhao, J., 2018. An overview of operating parameters and conditions in hydrocyclones for enhanced separations. Sep. Purif. Technol. 206, 268–285. https://doi.org/10.1016/j.seppur.2018.06.015.
Wang, R., Zhang, Z., Yan, X., Zhang, H., Wang, L., 2024. Hydrocyclone separation enhancement of fine particles based on interface control. Miner. Eng. 209, 108628. https://doi.org/10.1016/j.mineng.2024.108628.
Xing, L., Guan, S., Gao, Y., Jiang, M., 2023. Measurement of a three-dimensional rotating flow field and analysis of the internal oil droplet migration. Energies 16 (13), 5094. https://doi.org/10.3390/en16135094.
Xing, L., Jiang, M., Zhao, L., Gao, J., Liu, L., 2022. Design and analysis of de-oiling coalescence hydrocyclone. Separ. Sci. Technol. 57 (5), 749–767. https://doi.org/10.1080/01496395.2021.1945102.
Xu, B., Zhang, X., Zhao, L., Jiang, M., Liu, L., Xia, H., 2021. Structure design and preliminary experimental investigation on oil-water separation performance of a novel helix separator. Separ. Sci. Technol. 56 (15), 2680–2691. https://doi.org/10.1080/01496395.2020.1837874.
Yang, Z.M., He, Y.X., Xiang, Q., Zio, E., He, L.M., Luo, X.M., Su, H., Wang, J., Zhang, J.J., 2023. Gas liquid cylindrical cyclone flow regime identification using machine learning combined with experimental mechanism explanation. Pet. Sci. 20 (1), 540–558. https://doi.org/10.1016/j.petsci.2022.09.005.
Zhang, L., Lu, Z., Ma, L., Bai, Z., 2025. Experimental research on enhanced the microfine oil droplets separation using hydrocyclone coupled with fiber coalescence. Chin. J. Chem. Eng. https://doi.org/10.1016/j.cjche.2025.02.008.
Zhang, S., Zhao, L., Zhou, L., Liu, L., Jiang, M., 2023. Numerical and experimental study on enhanced oil–water separation performance using hydrocyclone coupled with particles. Phys. Fluids 35 (11). https://doi.org/10.1063/5.0177823.
Zhao, L., Wang, L., Zhang, S., Guo, Z., Lu, M., 2025. Impact of lipophilic particles on oil-water separation efficiency in hydrocyclones. Chem. Eng. Process 214, 110327. https://doi.org/10.1016/j.cep.2025.110327.
Zhou, H., Hu, Z., Zhang, Q., Wang, Q., Lv, X., 2019. Numerical study on gas-solid flow characteristics of ultra-light particles in a cyclone separator. Powder Technol. 344, 784–796. https://doi.org/10.1016/j.powtec.2018.12.054.
Zhou, J., Zhang, L., Hu, C., Li, Z., Tang, J., Mao, K., Wang, X., 2022. Calibration of wet sand and gravel particles based on JKR contact model. Powder Technol. 397, 117005. https://doi.org/10.1016/j.powtec.2021.11.049.